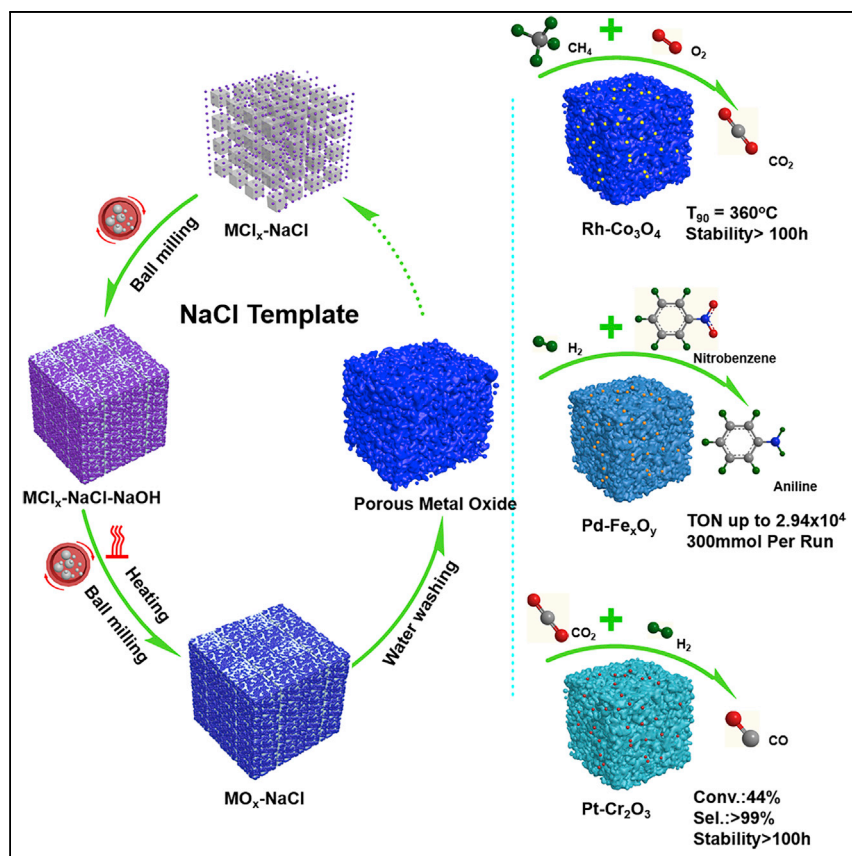


Article

A Principle for Highly Active Metal Oxide Catalysts via NaCl-Based Solid Solution



Yuan Shu, Hao Chen, Nanqing Chen, ..., Zhenghong Bao, Zili Wu, Sheng Dai

chemistryzpf@sjtu.edu.cn

HIGHLIGHTS

The NaCl-based solid solution could produce highly porous metal oxides

Noble metal species were simultaneously well-dispersed

The ion-sharing process of NaCl crystalline was completed by mechanochemistry

As-made $Rh\text{-Co}_3O_4$, $Pd\text{-Fe}_xO_y$, and $Pt\text{-Cr}_2O_3$ exhibited high catalytic performance

For industrial catalysis, a simple and green process for catalyst synthesis has always been pursued. In this regard, we utilized NaCl, one of the most common salts, as a template to prepare transitional metal oxide catalysts with both abundant porosity and well-dispersed noble metal species. Interestingly, this dispersion by NaCl was realized by solid-state grinding. Importantly, those catalysts afforded excellent performance in redox processes.

Article

A Principle for Highly Active Metal Oxide Catalysts via NaCl-Based Solid Solution

Yuan Shu,¹ Hao Chen,³ Nanqing Chen,³ Xiaolan Duan,¹ Pengfei Zhang,^{1,6,*} Shize Yang,^{4,5} Zhenghong Bao,² Zili Wu,² and Sheng Dai^{2,3}

SUMMARY

Toward the preparation of industrial metal oxide catalysts, **sacrificial organic templates, excessive solvents, complex impregnation, and drying steps are generally required.** Here, we report a versatile rule for the simple synthesis of highly porous metal oxides with well-dispersed noble metal species. Porous metal oxides (Co_3O_4 , Fe_xO_y , and Cr_2O_3) are obtained with some surface areas (e.g., Cr_2O_3 : $224 \text{ m}^2 \cdot \text{g}^{-1}$) beyond the record value. Surprisingly, small noble metal nanoparticles (e.g., Pd: 3.1 and Pt: 3.2 nm) could be incorporated by this solid-state process simultaneously. Corresponding Rh- Co_3O_4 , Pd- Fe_xO_y , and Pt- Cr_2O_3 exhibit excellent performance: CH_4 combustion ($T_{90} = \sim 360^\circ\text{C}$ and thermal stability: >100 h at 680°C), hydrogenation of nitrobenzene and derivatives (turnover number [TON] = 2.49×10^4 , 300 mmol per run), and reversed water gas shift (RWGS) reaction (44% CO_2 conversion with ~98% CO selectivity and thermal stability: >100 h at 500°C), respectively. Therefore, current principle via a NaCl-based solid solution could provide a solid-state, fast, and efficient route for processing metal oxide catalysts.

INTRODUCTION

Metal-oxide-based catalysts are of great importance in chemical industry. Toward the design of high-performance catalysts, the porous structure and dispersion of active phase are normally two key factors to be considered. It is well known that a high surface area is beneficial to the exposure of active sites, the adsorption, mass transfer, and desorption of the reactants, and so on.^{1–3} For example, porous manganese oxide catalyst showed excellent CH_4 combustion activity with T_{10} (temperature at which 10% CH_4 is converted) around 250°C , much lower than that (358°C) by commercial bulk Mn_2O_3 material.⁴ The dispersion of active phase is the other issue, mainly related to the size of noble metal nanoparticles (NPs). When the size is reduced to 1~3 nm, due to the integrated effects of increased low-coordinated surface atoms, surface relaxation, and quantum size effects, the performance of those catalysts would be generally improved.⁵ For instance, Au NPs with sizes between 0.5~5 nm showed high catalytic performance in CO combustion, but larger Au NPs are relatively inactive in the same process.^{6,7}

Controlling porous structure of metal oxides and dispersion of noble metal NPs usually require several steps. In general, porous metal oxides as supports or catalysts are synthesized by precipitation, solution combustion, or sol-gel methods to produce metal oxides with interstitial porosity. Meanwhile, metal oxides with

The Bigger Picture

Transition metal oxides (TMOs) are the most important catalysts in industrial chemistry. Tailoring the porosity of TMOs and the dispersion of active noble metal species are two strategies to enhance catalytic performance. However, the method of simultaneously producing porosity and high dispersion is quite scarce. Here, we propose a principle that NaCl-based solid solution could serve as a versatile platform to control both porosity and dispersion within TMO catalysts. The essence of this strategy lies in the ion-sharing talent of NaCl as a salt matrix by mechanochemistry, which promotes the high distribution of transition-metal precursors and noble metal species on NaCl crystalline. Besides, removing NaCl also releases pores. The corresponding TMO catalysts exhibit quite high catalytic performance in redox reaction.

well-defined and interconnected mesopores could be prepared by soft- or hard-templating methods.^{8–11} Based on self-assembly of organic surfactant aggregations and inorganic salt species, soft-templating technology greatly promotes the chemistry of mesoporous metal oxides, whereas several issues still remain, such as: excessive use of organic solvents, the long aging process from several days to a month, and the sacrificial behavior of surfactant molecules.¹² Meanwhile, hard-templating strategy has been well-mastered in the past few decades and provides a general solution to prepare mesoporous metal oxides.^{8,13,14} However, specific templates (e.g., Santa Barbara amorphous-15 [SBA-15], mobil composition of matter number 41 [MCM-41], and Korea Advanced Institute of Science and Technology number 6 [KIT-6]) as matrixes are necessary, and the removal of silica templates by hazardous chemicals (e.g., concentrated NaOH) adds an elaborate procedure, prompting researchers to explore alternative strategies. After acquiring porous supports, impregnation method (IMP) and deposition-precipitation method (DP) are typical methods to load and disperse noble metal NPs.^{15–17} In fact, the above-mentioned methods are rather successful in the construction of famous industrial catalysts, yet several issues still have not been well resolved. To date, the direct preparation of metal oxide catalysts with plentiful pores and well-dispersed noble metal species is highly desirable—from the standpoint of both fundamental and industrial catalysis.

As a powerful synthesis tool, mechanochemistry has shown attractive efficiency in the synthesis of zeolites,^{18–20} single-atom catalysts (SACs),²¹ organic molecules,^{22–25} MOF,²⁶ COF,²⁷ carbon,²⁸ and supported metal oxides.^{29–32} Based on our previous works on porous metal oxides by solid grinding method^{33–35} and inspired by the excellent solid solubility of NaCl,^{28,36–40} we questioned whether NaCl can serve as a salt template to direct porosity and at the same time dilute noble metal ions (e.g., Pd²⁺) in solid state. More encouragingly, a three-dimensional (3D) printing strategy of utilizing NaCl together with surfactants and solvents has already been reported for the fabrication of Mg scaffolds with well-controlled porosity.⁴¹ In this research, via a versatile NaCl-based solid solution, we reported a general principle for a simple preparation of highly porous metal oxides and related noble metal catalysts. Current synthesis is in fact different from the traditional molten salt method,^{42–44} as reflected by the following features: the calcination temperature (300°C) is far below the melting point of NaCl (~801°C) or related freezing points (e.g., freezing points of NaCl-CoCl₂ and NaCl-FeCl₃ at NaCl/(MCl_x+NaCl) (mol/mol) = 0.81 were 690°C and 772°C, respectively.⁴⁵). The NaCl-MCl_x solid solution is formed by mechanochemically grinding in solid state. After calcination, and removing and recycling NaCl by washing in water, a series of porous metal oxides (Fe_xO_y, Cr₂O₃, and Co₃O₄) were successfully synthesized, and the special surface area (SSA) of Cr₂O₃ (224 m²/g) is a record value.⁴⁶ Surprisingly, a family of bulky precious metal precursors could be processed into nano- or sub-nano scale by this solid state NaCl-diluting approach only. The preferred porosity and dispersion of those catalysts (Pd-Fe_xO_y, Pt-Cr₂O₃, and Rh-Co₃O₄) endow them with excellent activity and stability in various redox reactions, including: Rh-Co₃O₄ in CH₄ combustion (T₉₀ = 360°C, Stability at 680°C >100 h), Pd-Fe_xO_y in nitrobenzene hydrogenation (TON = 2.49 × 10⁴, 300 mmol Per Run), and Pt-Cr₂O₃ in CO₂ hydrogenation (conversion [Conv]: 44%, selectivity [Sel.] for CO: 98%; Stability at 500°C >100 h).

RESULTS AND DISCUSSION

Synthesis and Characterization of Mesoporous Metal Oxides

To verify the hypothesis if alkali metal-based solid solution could be used as a porosity-directing additive, we initially investigated the solubility of cobalt chloride

¹School of Chemistry and Chemical Engineering, Shanghai Jiao Tong University, Shanghai 200240, China

²Chemical Sciences Division, Oak Ridge National Laboratory, Oak Ridge, TN 37831, USA

³Department of Chemistry, University of Tennessee, Knoxville, TN 37996, USA

⁴Materials Science and Technology Division, Oak Ridge National Laboratory, Oak Ridge, TN 37831, USA

⁵Brookhaven National Laboratory, Upton, New York, NY 11973, USA

⁶Lead Contact

*Correspondence: chemistryzpf@sjtu.edu.cn
<https://doi.org/10.1016/j.chempr.2020.04.003>

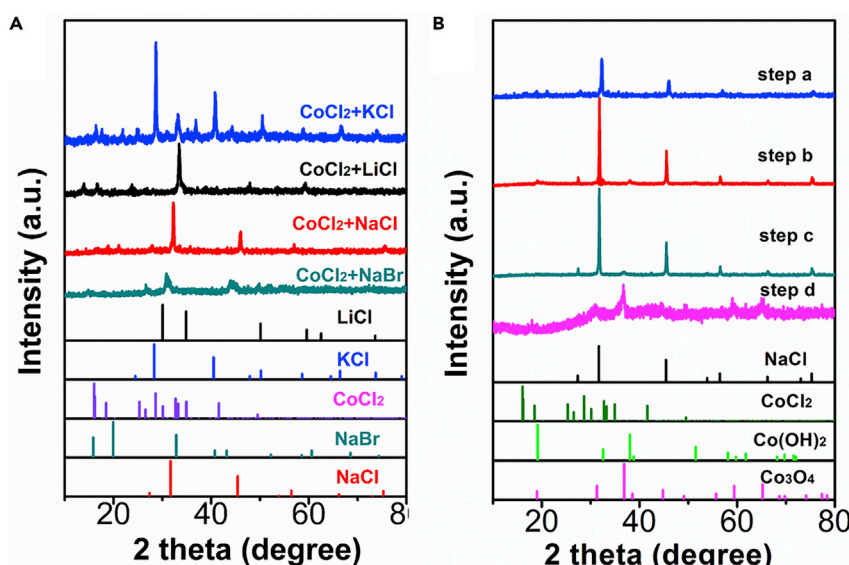


Figure 1. XRD Patterns of Salt Mixtures

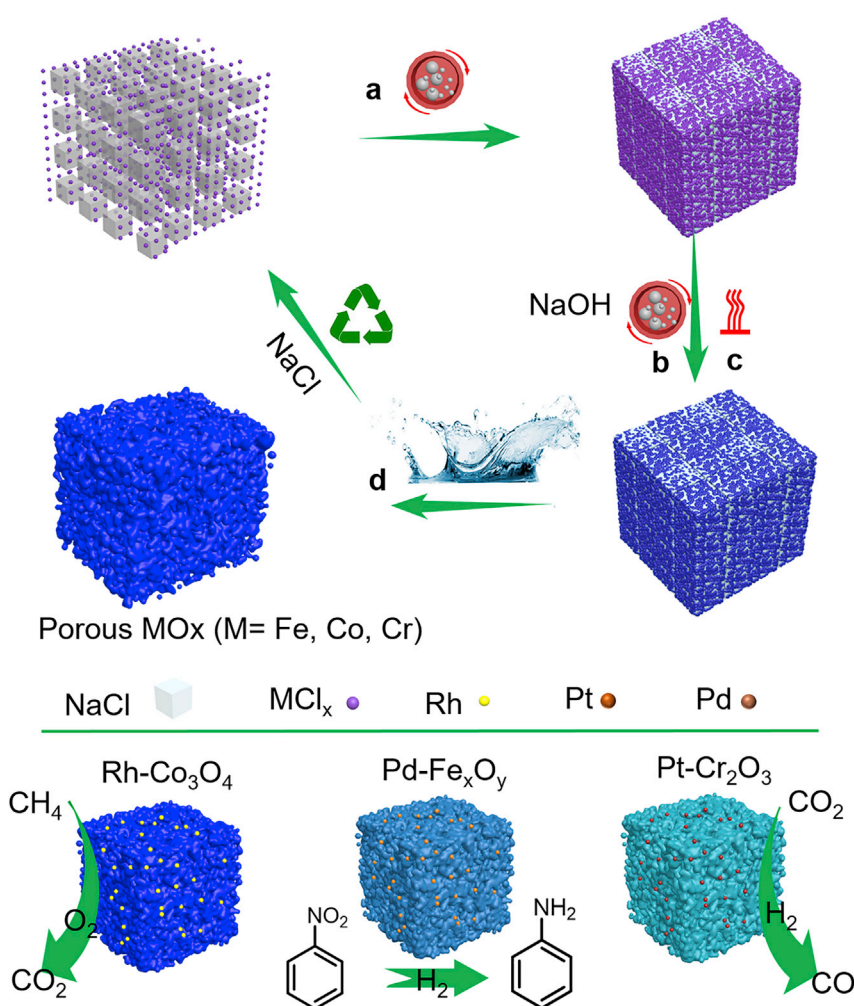
(A) XRD patterns of the mixture by ball milling CoCl₂ and alkali metal salts (NaCl, KCl, LiCl, or NaBr).

(B) XRD patterns of the intermediate products.

Step a. ball milling NaCl and CoCl₂; Step b. ball milling the mixture with NaOH; Step c. calcination in air; Step d. recycling NaCl by washing in water.

(CoCl₂) in several alkali metal salts (e.g., KCl, NaCl, LiCl, and NaBr) with different ionic radii. Typically, after ball milling of salt mixtures (e.g., CoCl₂-NaCl in ~1/1wt %) for 0.5 h, the intermediate product was immediately characterized by X-ray diffraction (XRD). Interestingly, when the solvent was NaCl ($a = 5.67 \text{ \AA}$), the XRD exhibited a group of typical peaks (27.3°, 31.7°, 45.5°, and 56.5°) for NaCl (Joint Committee on Powder Diffraction Standards Number [JCPDS NO.] 05-0628). No XRD peaks relating to CoCl₂ were detected, indicating that Co²⁺ cations were well-dispersed in the solid NaCl lattice (See Figure 1A). On the contrary, with KCl as the diluter, the XRD pattern showed multi peaks for both KCl (JCPDS NO. 41-1476) and CoCl₂ (JCPDS NO. 72-2408). The larger lattice parameter ($a = 6.29 \text{ \AA}$) of KCl might have led to this mismatching behavior of KCl-CoCl₂ crystals. Similar observations occurred in the cases of CoCl₂-LiCl ($a = 5.14 \text{ \AA}$) and CoCl₂-NaBr ($a = 5.97 \text{ \AA}$), whose diffraction patterns evidently deviated from the precursors. Among the salts studied above, NaCl seems like a suitable solid solvent for diluting and restructuring CoCl₂.

The mechanochemical synthesis of porous metal oxides via NaCl-based solid solution was shown in Scheme 1, and each step was carefully studied by XRD (Figure 1B). At the beginning, the mixing of NaCl (0.5–2 g) and CoCl₂ (0.475 g) was promoted by ball milling. After the homogeneous dispersion of Co²⁺ cations, stoichiometric NaOH as the oxygen donor was added into the mixture. Because of the strong Coulomb interaction between Co²⁺ and OH⁻ ($K_{sp}\text{-}\alpha\text{-Co(OH)}_2 = 1.09 \times 10^{-15}$),⁴⁷ the selective transformation of Co²⁺ to the corresponding hydroxide occurred, which was evidenced by the presence of characteristic peaks for Co(OH)₂ (JCPDS NO. 74-1057). The weak XRD intensity of Co(OH)₂ suggested that the solid state coordination between Co²⁺ and OH⁻ might undertake around the NaCl crystalline matrix. Interestingly, after calcination of Co(OH)₂ into Co₃O₄, strong XRD peaks for NaCl with poor responses for Co₃O₄ were observed in the mixture, revealing the good dispersion of Co₃O₄ species. Finally, the NaCl template was removed



Scheme 1. General Synthesis of Porous Metal Oxides and Corresponding Supported Metal Oxides through NaCl-Based Solid Solution

(A) Ball milling a mixture of NaCl particles and transition metal precursors in 0.5 h.

(B) Ball milling the intermediate together with NaOH in 0.5 h.

(C) Calcination in air.

(D) Recycling NaCl by washing in water.

The bottom part shows three as-made catalysts and their application in model redox reactions.

and recycled by washing in water, accompanied by the release of porosity. The XRD pattern of resulting Co₃O₄ sample (See Figures 1B and S1) showed five broad peaks at 31.1°, 36.6°, 49.1°, 59.3°, and 65.1°, corresponding to the (111), (220), (311), (400), (511), and (440) planes of cubic phase Co₃O₄ (JCPDS NO. 43-1003), respectively. The average crystal size of the Co₃O₄ estimated by Scherrer's equation was 12.1 nm.

The SSAs of Co₃O₄ samples synthesized with different salts (KCl, NaCl, LiCl, CsCl, NaBr, and NaNO₃) were evaluated by nitrogen sorption measurements at 77 K. From Figure 2A; Table 1, we can see that the type of dilute salts has an important influence on the SSA value. The NaCl-derived Co₃O₄ (NaCl) sample had a good SSA of 110 m²/g, meanwhile its sorption curve exhibited a typical type IV isotherm with a H₃-type hysteresis loop between relative pressure P/P₀ = ~0.5–1.0, implying

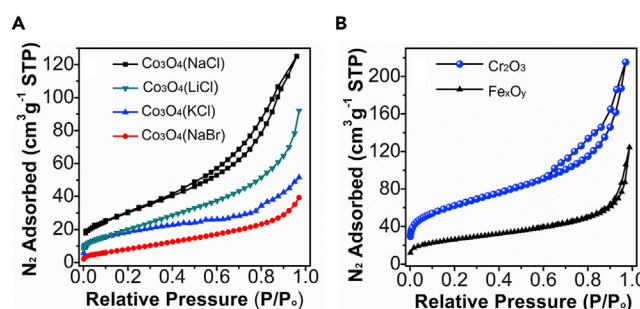


Figure 2. N_2 Adsorption Curves of Porous Metal Oxides

(A) N_2 sorption isotherms (77K) of Co_3O_4 samples synthesized by different solid salts.

(B) N_2 sorption isotherms (77K) of Cr_2O_3 and Fe_xO_y obtained by NaCl method.

Synthetic condition: transition metal salts 2 mmol, NaCl 0.5 g, stoichiometric NaOH 4 mmol or 6 mmol, and calcination temperature 300°C.

the formation of interstitial mesopores. However, control synthesis of Co_3O_4 without NaCl resulted in a decrease in SSA calculated by Brunner-Emmet-Teller (BET) method (Co_3O_4 -blank with $70\text{ m}^2/\text{g}$). On the other hand, when LiCl, KCl, CsCl, or NaBr were used as the solid solvent, the SSAs of Co_3O_4 samples decreased to 74, 67, 37, and $31\text{ m}^2/\text{g}$, respectively. This trend somewhat supports the observation by XRD, and the formation of $CoCl_2$ -NaCl solid solution could contribute more porosity into Co_3O_4 . In addition, the amount of NaCl additive (0–4 g) had a moderate effect on SSA of Co_3O_4 , and the BET SSAs of Co_3O_4 by different NaCl dosages followed the sequence of Co_3O_4 -2 g: $116\text{ m}^2/\text{g}$, Co_3O_4 -0.5 g: $110\text{ m}^2/\text{g}$, Co_3O_4 -4 g: $86\text{ m}^2/\text{g}$, and Co_3O_4 -0 g: $70\text{ m}^2/\text{g}$. Therefore, 0.5 g NaCl was selected as the appropriate dosage to transforming 2 mmol $CoCl_2$ (0.475 g) into porous Co_3O_4 . In fact, the dosage of NaCl (0.5 g) is low compared with the molten salt method, during which salt additives with 10–20 dosages by weight were generally needed.^{42–44} By the way, the current calcination temperature (300°C) was lower than the freezing point of NaCl- $CoCl_2$ at $NaCl/(CoCl_2+NaCl)$ (mol/mol) = 0.81 (690°C),⁴⁵ and thus the current process was undergone in solid state. The calcination temperature (300°C) is similar to those by precipitation method, impregnation method and deposition-precipitation method, thus the energy consumption of this method is comparable to that of other traditional methods.

In order to study the scope of this method, two other metal oxides (Fe_xO_y and Cr_2O_3) were prepared by using NaCl as the salt template. The crystal phases of Fe_xO_y and Cr_2O_3 were confirmed by XRD (See Figure S1). The Fe_xO_y sample exhibited eight peaks at 18.3° , 24.1° , 30.1° , 33.1° , 35.4° , 53.4° , 56.9° , and 62.5° , among which those peaks located at 24.1° and 33.1° belonged to (104) and (012) planes of Fe_2O_3 (JCPDS NO.89-0597), and the other peaks corresponded to (111), (220), (311), (422), (511), and (440) planes of Fe_3O_4 (JCPDS NO.79-0419), respectively. Thus, the sample was a mixture of Fe_2O_3 and Fe_3O_4 . The Cr_2O_3 sample showed six clear peaks which were assigned to the (104), (110), (202), (024), (214), and (300) planes of Cr_2O_3 (JCPDS NO.84-0312). The average crystal sizes of Fe_xO_y and Cr_2O_3 by Scherrer's equation were 21 and 13 nm, implying that Fe and Cr precursors also could be well-dispersed on NaCl solid matrix.

By the N_2 sorption isotherms at 77 K, the SSAs of these metal oxides were quite high (Fe_xO_y : $100\text{ m}^2/\text{g}$, Cr_2O_3 : $224\text{ m}^2/\text{g}$), whereas those of Fe_xO_y and Cr_2O_3 obtained without NaCl were much lower (Fe_xO_y -blank: $53\text{ m}^2/\text{g}$, Cr_2O_3 -blank: $73\text{ m}^2/\text{g}$), further proving the importance of a NaCl template (Table 1). The BET SSA of Cr_2O_3 sample

Table 1. BET Surface Areas of Corresponding Metal Oxides

Sample	Salt	Source	Noble Metal	SSA (m^2/g) ^a
Co_3O_4 -Blank	N/A	CoCl_2	N/A	70
Co_3O_4	NaCl (0.5 g)	CoCl_2	N/A	110
Co_3O_4	LiCl (0.5 g)	CoCl_2	N/A	67
Co_3O_4	KCl (0.5 g)	CoCl_2	N/A	74
Co_3O_4	NaBr (0.5 g)	CoCl_2	N/A	31
$\text{Co}_3\text{O}_4\text{-CsCl}$	CsCl (0.5 g)	CoCl_2	N/A	37
$\text{Co}_3\text{O}_4\text{-NO}_3^{\text{b}}$	NaNO_3 (0.5 g)	CoCl_2	N/A	99
$\text{Co}_3\text{O}_4\text{-2g}$	NaCl (2 g)	CoCl_2	N/A	116
$\text{Co}_3\text{O}_4\text{-4g}$	NaCl (4 g)	CoCl_2	N/A	86
Fe_xO_y -Blank	N/A	FeCl_3	N/A	53
Fe_xO_y	NaCl (0.5 g)	FeCl_3	N/A	100
$\text{Fe}_x\text{O}_y\text{-NO}_3^{\text{b}}$	NaNO_3 (0.5 g)	FeCl_3	N/A	249
Cr_2O_3 -Blank	N/A	CrCl_3	N/A	73
Cr_2O_3	NaCl (0.5 g)	CrCl_3	N/A	224
$\text{Cr}_2\text{O}_3\text{-NO}_3^{\text{b}}$	NaNO_3 (0.5 g)	CrCl_3	N/A	191
Rh-Co ₃ O ₄	NaCl (0.5 g)	CoCl_2	RhCl_3	142
Pd-Fe _x O _y	NaCl (0.5 g)	FeCl_3	PdCl_2	172
Pt-Cr ₂ O ₃	NaCl (0.5 g)	CrCl_3	H_2PtCl_6	111

^aSSA calculated by using the BET equation.

^bThe NaNO_3 template was decomposed during calcination at 300°C.

(224 m^2/g) is a record value to the best of our knowledge (Cr_2O_3 obtained by pyrolysis of MIL-101-Cr: 77.4 m^2/g ,⁴⁸ Cr_2O_3 by using KIT-6 or SBA-15 as hard-templating: 70~ 92 m^2/g ,^{49,50} Cr_2O_3 synthesized by CTAB as template: 125–143 m^2/g ⁵¹). Moreover, NaNO_3 also functioned well for generating porosity into metal oxides ($\text{Co}_3\text{O}_4\text{-NO}_3$, $\text{Fe}_x\text{O}_y\text{-NO}_3$, and $\text{Cr}_2\text{O}_3\text{-NO}_3$ were 99, 249, and 191 m^2/g). However, NO_3^- ions would be decomposed during calcination (300°C), therefore NaNO_3 cannot be recycled and reused. Based on those results, NaCl seems like a better choice for the synthesis of porous metal oxide.

To study the macroscopic morphology of those metal oxide catalysts, we carefully performed scanning electron microscopy (SEM) characterization (see Figure 3). Those metal oxides (Co_3O_4 , Cr_2O_3 , and Fe_xO_y) displayed coral reef-like structure, and apparent interstitial pores could be observed between aggregated particles. This morphology is somewhat similar with porous materials by ionothermal synthesis,^{52–54} during which metal oxides would form around NaCl solid solution and porous aggregations with small particles are left after the removal of NaCl.

Due to the excellent value in SSA, material morphology of the Cr_2O_3 sample was further observed by scanning transmission electron micrographs (STEM). As seen from Figure 4A, a sponge-like nanostructure with plentiful and continuous pores can be observed throughout the bulky aggregation in several micrometers. More clear views of the porous structure were observed by combining high-resolution high angle annular dark field (HAADF) image and corresponding bright field (BF) image (See Figure S2). The apparent mesopores with diameters around 3–15 nm could be found side by side, which roughly coincided with the pore size distribution by the Barret-Joyner-Halends (BJH) model using N_2 adsorption branch (See

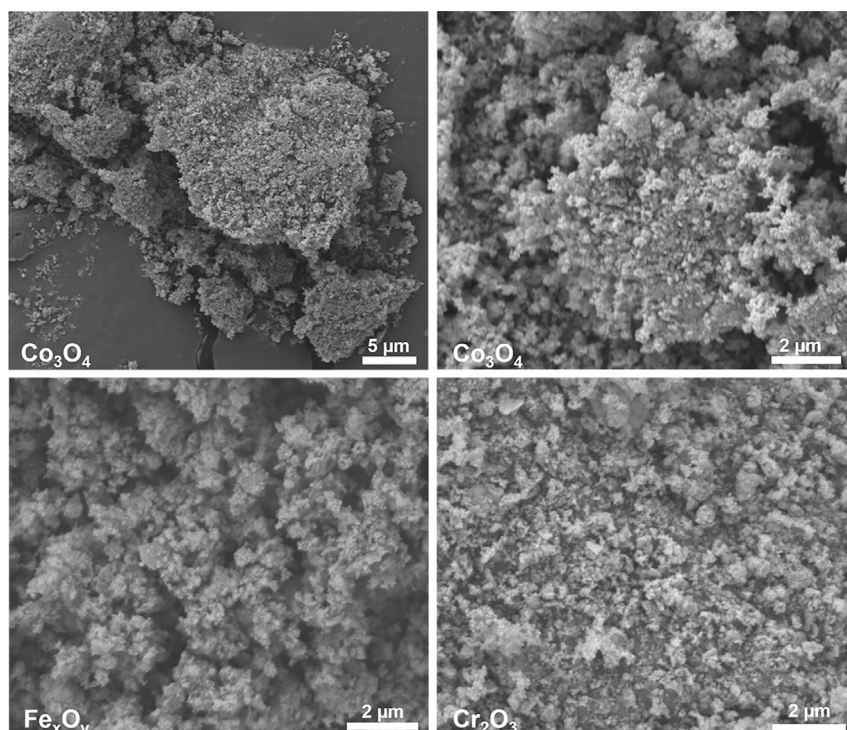


Figure 3. SEM Images of Porous Metal Oxides (Co_3O_4 , Fe_xO_y , and Cr_2O_3)

(See Figure S3). The irregular accretion of tiny Cr_2O_3 NPs mainly contributed to the formation of porosity. The crystalline of Cr_2O_3 was further checked by high-resolution transmission electron microscopy (HRTEM) (See Figure 4B), and the found spacings of lattice fringes were 0.23 and 0.26 nm, which agreed well with the (113) and (104) crystal planes of Cr_2O_3 , respectively.⁴⁹ These data demonstrate that current strategy using NaCl-based solid solution can produce porous metal oxides with high surface areas.

Encouraged by the porosity-directing ability of this method, NaCl-based solid solution was extended to dilute noble metal species. The initial solid solution was formed by ball grinding NaCl, transitional metal chlorides, and noble metal chlorides. Several catalysts (Rh- Co_3O_4 , Pd- Fe_xO_y , and Pt- Cr_2O_3) can be obtained after calcination and the removal of NaCl. XRD was used to characterize the crystalline phases of Pd, Rh, and Pt on Pd- Fe_xO_y , Rh- Co_3O_4 , and Pt- Cr_2O_3 , respectively. With Pt- Cr_2O_3 as an example, those peaks can be well-indexed to typical cubic phase of Cr_2O_3 (See Figure S4). Although Pt content by inductively coupled plasma atomic emission spectrometry (ICP-AES) was quite high (9.4 wt %), no clear diffraction peaks relating to Pt species were observed in the sample of Pt- Cr_2O_3 , indicating the good dispersion of Pt NPs on the Cr_2O_3 support. The morphology and size of Pt species were further characterized by STEM-HAADF images. According to the Figures 4C, 4D, and S5, the Pt NPs were homogeneously anchored over the Cr_2O_3 support in the domain of several hundred nanometers and the average size of Pt NPs was 3.2 nm. However, further dilution of precious metal chloride by increasing the proportion of NaCl did not effectively reduce the size of Pt NPs (~3.5 nm) (See Figure S6).

For Pd- Fe_xO_y and Rh- Co_3O_4 catalysts, the typical peaks of Pd and Rh species were also absent in the corresponding XRD patterns, suggesting the high dispersion

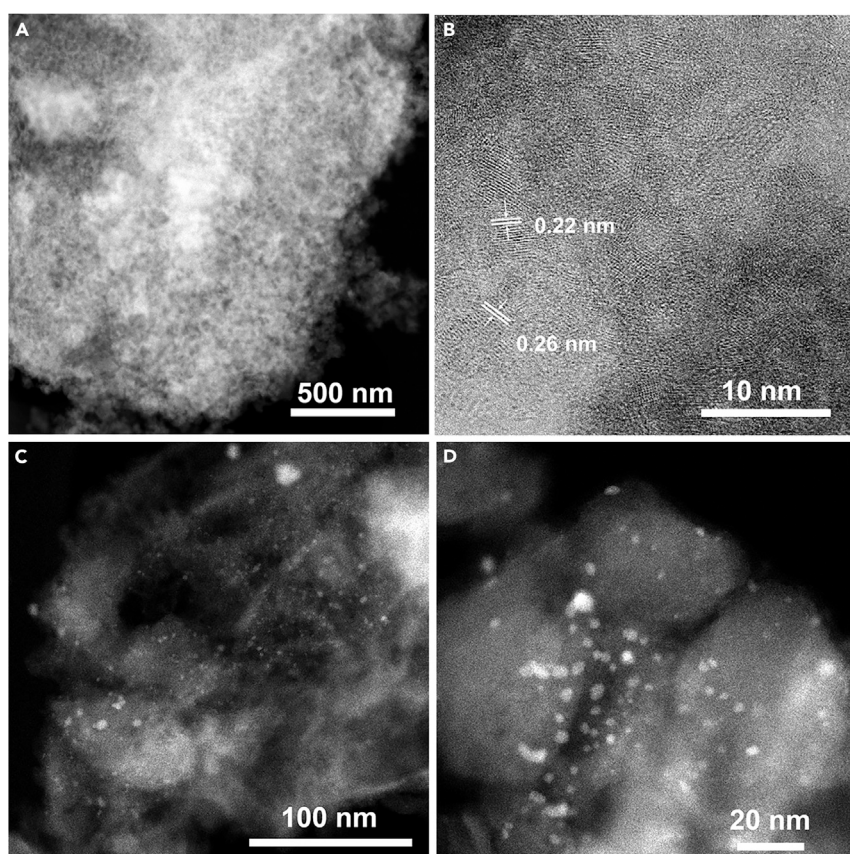


Figure 4. Morphology of Cr_2O_3 and $\text{Pt}-\text{Cr}_2\text{O}_3$ Catalysts.
STEM-HAADF images of Cr_2O_3 (A and B) and $\text{Pt}-\text{Cr}_2\text{O}_3$ (C and D). See also Figure S5.

of Pd and Rh species. The STEM images of $\text{Pd}-\text{Fe}_x\text{O}_y$ material were collected in Figures 5A, 5B, and S7, which displayed honeycomb-like matrix with abundant pores from surface to interior. Pd NPs with an average size of 3.1 nm decorated the surface, and the Pd loading was 6.3 wt % by ICP-AES. Besides, the well-dispersion of Pd NPs was directly observed by the energy dispersive X-ray spectrometry (EDX) elemental mapping images of Pd and Fe species (See Figures 5C–5E). As to $\text{Rh}-\text{Co}_3\text{O}_4$ catalyst, no Rh NPs were observed in the STEM images of $\text{Rh}-\text{Co}_3\text{O}_4$ even though we have tried many different areas of copper mesh (See Figure S8). But ICP-AES spectrum of $\text{Rh}-\text{Co}_3\text{O}_4$ showed the presence of Rh element (Rh: 7.6 wt %). Based on the results above, it seems fair to say that the NaCl-based solid-solution functions well for dispersing noble metal species within oxide catalyst.

By IMP or DP methods, loading active components into metal oxides usually leads to the blockage of porous channels, which in turn causes a decrease in the SSA of the carrier. This issue could be somewhat avoided in current method. For example, the SSAs of $\text{Rh}-\text{Co}_3\text{O}_4$ ($142 \text{ m}^2/\text{g}$) and $\text{Pd}-\text{Fe}_x\text{O}_y$ ($172 \text{ m}^2/\text{g}$) were higher than that of Co_3O_4 ($110 \text{ m}^2/\text{g}$) and Fe_xO_y ($100 \text{ m}^2/\text{g}$), respectively. The synthetic steps (e.g., milling parameters, grinding time, calcination temperature, and washing steps) for metal oxides and noble metal loaded metal oxides were almost identical, whereas the addition of noble metal chloride or not was different. Therefore, the increased surface areas for supported catalysts can be ascribed to the enhanced dispersion effect by noble metal species.

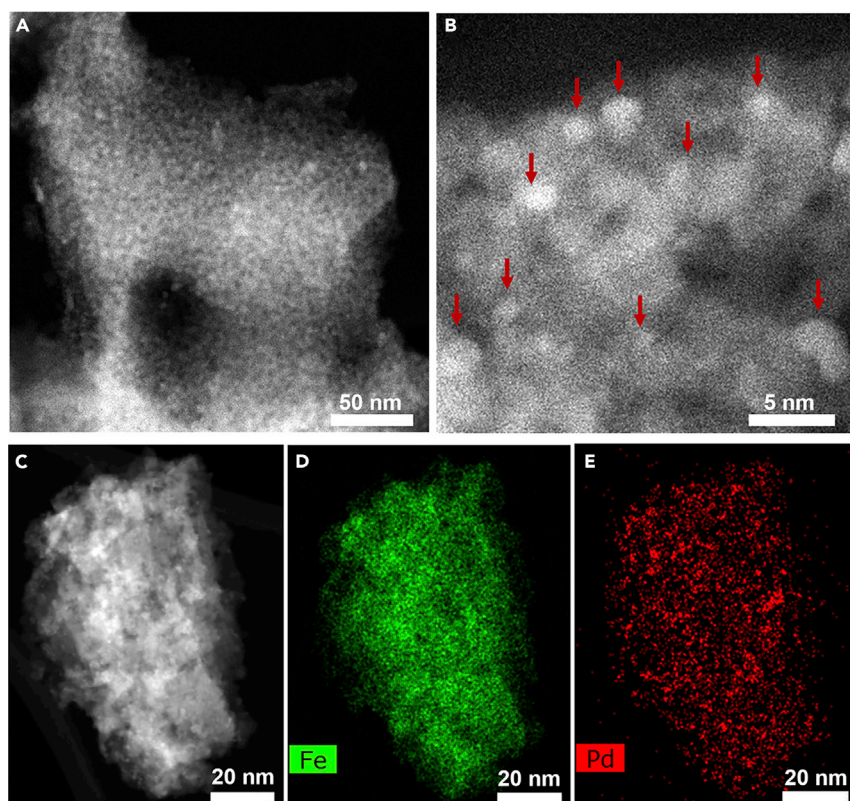


Figure 5. STEM Images and EDS Mapping Images of $\text{Pd-Fe}_x\text{O}_y$

(A and B) are STEM images of $\text{Pd-Fe}_x\text{O}_y$ with scale bar at 50 and 5 nm, respectively.

(C) STEM image of $\text{Pd-Fe}_x\text{O}_y$.

(D) Fe EDX elemental mapping image for $\text{Pd-Fe}_x\text{O}_y$ catalyst.

(E) Pd EDX elemental mapping image for $\text{Pd-Fe}_x\text{O}_y$ catalyst.

See also Figure S7.

Normally, with the high dispersion of noble metal on the support, the interaction between support and noble metal is always interesting.⁵⁵ Therefore, a series of H₂-temperature programmed reduction (H₂-TPR) spectra of Rh-Co₃O₄, Pt-Cr₂O₃, and Pd-Fe_xO_y were performed (See Figure S9). As for Rh-Co₃O₄ and Pt-Cr₂O₃, two evident reduction peaks prior to 150°C were attributed to the reduction of Rh species and Pt species (Rh: ~125°C, Pt: ~118°C), due to the strong redox capacity of RhO_x and PtO_x. The peaks at 223°C and 187°C were assigned to the reduction of the Co₃O₄ and Cr₂O₃, respectively, whereas the reduction of pure Co₃O₄ and Cr₂O₃ occurred at ~360°C^{56,57} and ~310°C,⁵⁸ respectively. This decreased reduction temperature indicates that preferred contact or interaction between noble metal species and Co₃O₄ or Cr₂O₃. As for Pd-Fe_xO_y, no PdO reduction peak could be observed, possibly due to the reduction of Pd oxides before measurement temperature.⁵⁹ The reduction peak around 320°C could be attributed to the reduction of Fe₂O₃.⁶⁰

Catalytic Performance of Catalysts

The Pd-Fe_xO_y, Pt-Cr₂O₃, and Rh-Co₃O₄ materials developed by this NaCl solid-solution method possessed high SSAs and well-dispersed noble metal NPs, which were supposed to show good catalytic performance. Then, we chose three important redox processes as model reactions to evaluate their activity.

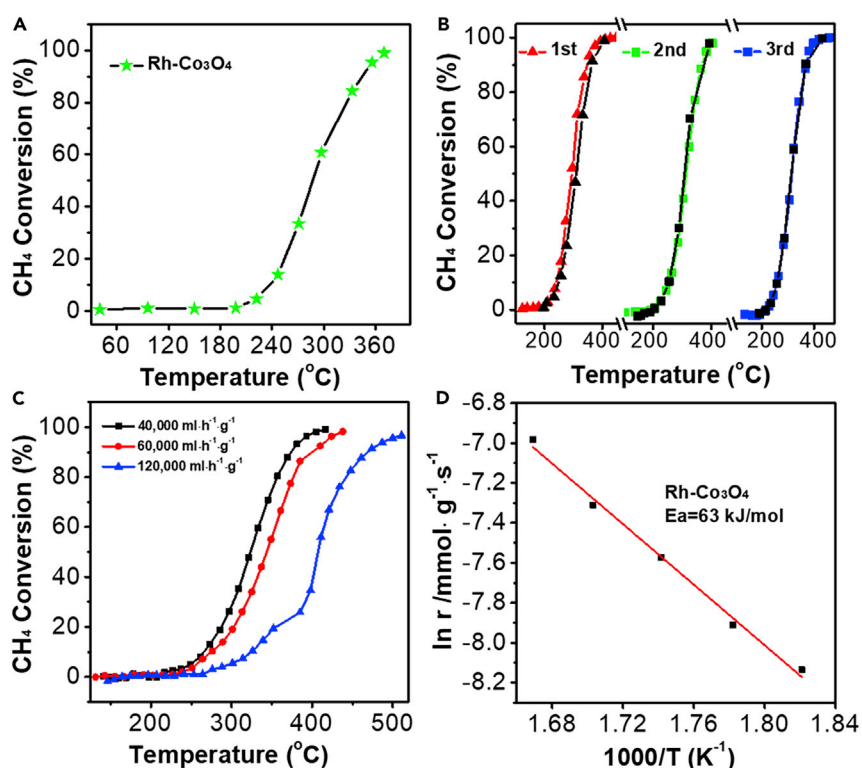


Figure 6. CH₄ Combustion Performance of Rh-Co₃O₄

- (A) The CH₄ (1% in air) combustion curve over Rh-Co₃O₄ under 20,000 mL·h⁻¹·g⁻¹.
(B) Light-off curves of methane combustion for Rh-Co₃O₄ in three heating-cooling cycles (1% CH₄ in air under 20,000 mL·h⁻¹·g⁻¹). Color line, heating part of the cycle; black line, cooling part of the cycle.
(C) The CH₄ (1% in air) combustion curves over Rh-Co₃O₄ under increased weight hourly space velocities.
(D) Arrhenius plots of the reaction rate (ln r) versus 1/T for CH₄ combustion over Rh-Co₃O₄.

CH₄ Combustion

Emission of low concentration methane from natural gas vehicle and coal mine is becoming an urgent issue, because of its low explosive limit in air and the strong greenhouse effect of methane.⁶¹ Toward this end, catalytic combustion of methane at low temperature is an effective strategy.⁶² Because Co₃O₄ has a spinel structure, valence states of transition-metal cations in either tetrahedral or octahedral interstices are variable, and the surface lattice oxygen anions have different coordination numbers, which results in different Lewis basic sites on the surface.⁶³ These unique characteristics endow Co₃O₄ with excellent catalytic activity in combustion reaction. In order to improve the performance of cobalt-based catalysts, the usual strategy is to optimize the crystal surface and SSA of Co₃O₄, and supported active noble metal NPs.^{63–65} In fact, Rh and Pd are next to each other in the periodic table of elements, Rh exhibits similar activity to Pd in catalytic combustion but with better thermal durability.^{66–68} Therefore, the porous Rh-Co₃O₄ with a high SSA value was investigated in methane combustion.

As shown in Figure 6, Rh-Co₃O₄ afforded a good activity in catalytic combustion of CH₄. The ignition temperature T₁₀ (at which temperature 10 % methane was converted) of Rh-Co₃O₄ was relatively low, only 260°C. Beyond T₁₀, CH₄ conversion rapidly increased, whereas the total oxidation was complete at 370°C (T₉₉). To

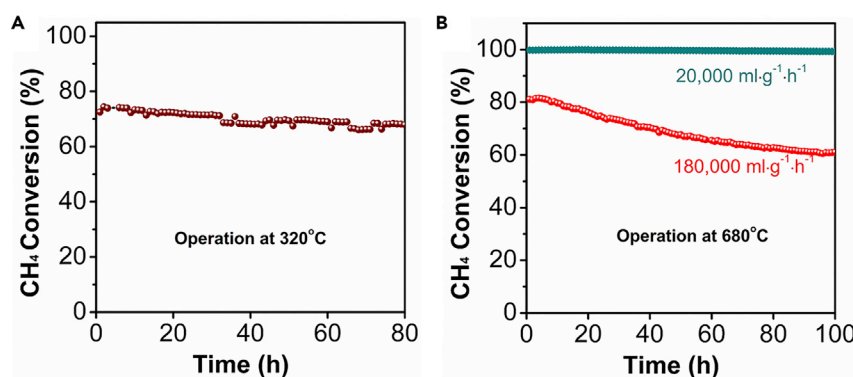


Figure 7. Stability Tests of Rh-Co₃O₄

(A and B) Shown in (A) and (B) are the stability tests of Rh-Co₃O₄ under 320°C and 680°C, respectively. Reaction conditions: WHSV of (A) is 20,000 mL·g⁻¹·h⁻¹ and WHSVs of (B) are 20,000 mL·g⁻¹·h⁻¹ and 180,000 mL·g⁻¹·h⁻¹, respectively.

evaluate the stability, we then reused Rh-Co₃O₄ three times under cooling-heating cycles between 100°C and 450°C. The heating portions of three conversion curves in Figure 6B exhibited similar T₉₀ values, 366°C for 1st, 370°C for 2nd, and 371°C for 3rd. Besides, among all light-off cycles, the curves of cooling and heating part were close to coincident, implying the kinetic transformation of CH₄ was stable at varied temperature.

To further evaluate the activity of Rh-Co₃O₄, we tested CH₄ light-off curves under various weight hourly space velocities (WHSVs). As shown in Figure 6C, the catalytic performance was almost maintained with the increase of WHSV from 20,000 mL·g⁻¹·h⁻¹ to 40,000 and 60,000 mL·g⁻¹·h⁻¹, which was evident by the similar light-off curves. When continuing to increase WHSV to 120,000 mL·g⁻¹·h⁻¹, the CH₄ conversion began to decrease, and the T₉₀ shifted to 469°C. In view that the external diffusion limitation can be overlooked under high WHSV, the calculation of activation energy (E_a) was undertaken by using the CH₄ conversion data (CH₄ conversion between 5% and 15%) at 120,000 mL·g⁻¹·h⁻¹. The calculated E_a was 63 kJ·mol⁻¹ (See Figure 6D), which was comparable to Pd-based excellent catalysts.^{69,70} A more comprehensive comparison of the performance of Rh-Co₃O₄ and other catalysts was shown in Table S1, whereas this Rh-Co₃O₄ synthesized via mechanochemical NaCl-templated method exhibits good catalytic activity.

CH₄ combustion catalysts are often used in high temperature, therefore a good thermal stability is required. Although Pd-based catalysts are excellent in CH₄ combustion, stability has always been a difficult issue because of the sintering of active Pd species and the decomposition of PdO at high temperatures.⁷¹ In general, the sintering problem could be modified by the introduction of metal NPs with higher melting points.⁷² With a melting point of 1,955°C (metallic Rh), the thermal stability of Rh-Co₃O₄ was then studied in detail (Figure 7A). After continuous operation at 320°C for 80 h, Rh-Co₃O₄ exhibited a fairly stable performance, there was no significant change in the conversion of methane. In order to further investigate the potential of Rh-Co₃O₄, we raised the reaction temperature to 680°C and evaluated its high temperature stability. Under a low WHSV (20,000 mL·g⁻¹·h⁻¹), Rh-Co₃O₄ remained 100% CH₄ conversion during continuous combustion for 100 h (See Figure 7B). The stability of Rh-Co₃O₄ was further investigated under a high WHSV (180,000 mL·g⁻¹·h⁻¹). Although the reaction condition was rather harsh (high WHSV: 180,000 mL·g⁻¹·h⁻¹ and high temperature: 680°C), the Rh-Co₃O₄

Table 2. Hydrogenation of Nitrobenzene under Different Conditions

Entry	Catalyst (mg)	Temp. (°C)	Solvent	Conv. (%) ^a
1	20	60	ethanol	41
2	20	70	ethanol	94
3	20	90	ethanol	>99
4	20	70	methanol	>99
5	20	70	H ₂ O	>99
6	20	50	H ₂ O	>99
7	20	30	H ₂ O	84
8	10	30	H ₂ O	80

Abbreviations are as follows: Temp, Temperature; Conv, Conversion

^aReaction condition: solvent 20 mL, 5 mmol nitrobenzene, H₂ 10 bar, and reaction time 1 h.

still could keep 75% catalytic performance after 100 h (the lighting-off curve of CH₄ under a WHSV of 180,000 mL·g⁻¹·h⁻¹ was shown in [Figure S10](#)). With high CH₄ combustion activity and stability, the Rh-Co₃O₄ prepared from NaCl method is a promising system to treat low concentration methane.

Nitrobenzene Hydrogenation

Aniline is a key intermediate for the manufacture of polyurethane, indigo, and other industrial chemicals, whereas the selective hydrogenation of nitrobenzene is one of the most effective methods to produce aniline.⁷³ Pd catalysts supported on carbon, MCM-48 and mesoporous metal oxides (TiO₂, ZrO₂, and Al₂O₃) have been extensively studied with excellent hydrogenation performance, however, recycling the used palladium-containing catalysts is quite complex in liquid-phase hydrogenation.⁷⁴⁻⁷⁷ Magnetic separable material is an attractive heterogeneous catalyst because it is easy to be recycled, and then the current Pd-Fe_xO_y catalyst with magnetic feature, high surface area, and small Pd NPs was applied to the hydrogenation of nitrobenzene.

A preliminary attempt to optimize the hydrogenation process at different temperatures was carried out with ethanol as solvent. As the reaction temperature increased from 60°C to 90°C, a rapid increase of nitrobenzene conversion from 44% to >99% occurred ([Table 2](#)). Aniline was the sole found product, whereas side products such as nitrosobenzene, N-phenyl hydroxylamine, azoxybenzene, azobenzene, and hydrazobenzene cannot be detected on GC. To further improve the performance of Pd-Fe_xO_y, the effect of solvent in nitrobenzene hydrogenation was investigated. When the reaction temperature was fixed at 70°C, the conversions of nitrobenzene were 98% in methanol solvent and 100% in water. With H₂O as the green solvent, we continued to optimize the reaction temperature. When the temperature was reduced to nearly room temperature (30°C), the Pd-Fe_xO_y still exhibited good performance with an 85% conversion of nitrobenzene. Even when the amount of Pd-Fe_xO_y catalyst is halved, an 80% conversion of nitrobenzene still was preserved.

To study the scope of this Pd-Fe_xO_y catalyst, various derivatives of nitrobenzene such as o-Nitrotoluene, 4-nitrochlorobenzene, 4-nitroanisole, 1-Bromo-4-Nitrobenzene, and p-Nitrotoluene were hydrogenated at 50°C. As shown in [Table 3](#), all five derivatives with either electron-withdrawing or electron-donating groups were successfully hydrogenated to corresponding amines with high selectivity. Especially, the catalytic hydrogenation of o-Nitrotoluene, a molecule with steric hindrance, could be finished in 50 min, revealing the general activity of Pd-Fe_xO_y catalyst.

Table 3. Hydrogenation of Nitrobenzene Derivatives under Different Conditions

Entry	Substrate	Product	Time (min)	Conv. ^a	Sel. ^b
1			50	>99%	>99%
2			20	>99%	>99%
3			20	>99%	>99%
4			40	>99%	>99%
5			30	>99%	>99%

Reaction condition: solvent 20 mL, 5 mmol nitrobenzene derivative, and 20 mg Pd-Fe_xO_y. Temperature 50°C, H₂ 10 bar, and reaction time 1 h.

^aConv, conversion.

^bSel, selectivity.

To study the catalyst stability, spent Pd-Fe_xO_y solid was separated by the action of external magnet, which was reused for the next run. The Pd-Fe_xO_y catalyst was rather stable in the five cycles of hydrogenation reaction, during which the nitrobenzene conversions were kept around 68% (See Figure 8A). The dispersion of Pd NPs on the reused Pd-Fe_xO_y catalyst was explored by STEM-EDX mapping and electron energy loss spectroscopy (EELS) (See Figures 8B and S11). Pd NPs were well-dispersed on the Fe_xO_y support. The interaction between Pd NPs and Fe_xO_y might have contributed to the reaction stability of Pd-Fe_xO_y during nitrobenzene hydrogenation.

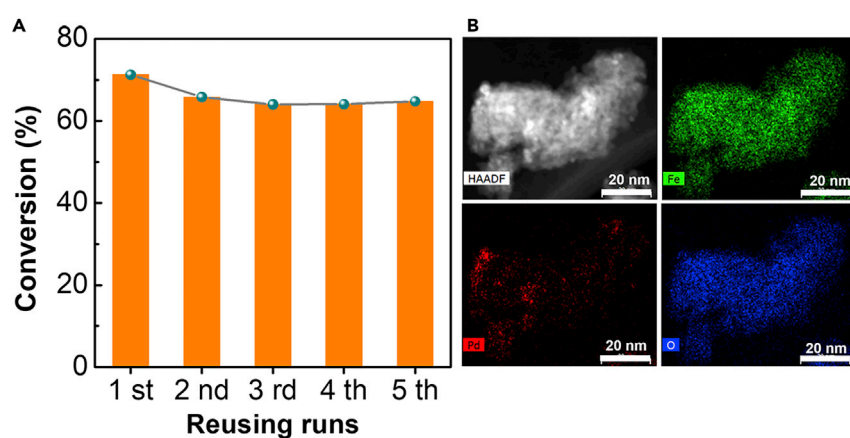


Figure 8. Stability Measurement of Pd-Fe_xO_y Catalyst in Nitrobenzene Hydrogenation

(A) Reusing runs of Pd-Fe_xO_y. Reaction condition: 20 mL H₂O, 20 mg Pd-Fe_xO_y (recycled), reaction time 1 h, 15 mmol nitrobenzene, temperature at 50°C, and H₂ 10 bar.

(B) STEM and EDX mapping images of the reused Pd-Fe_xO_y.

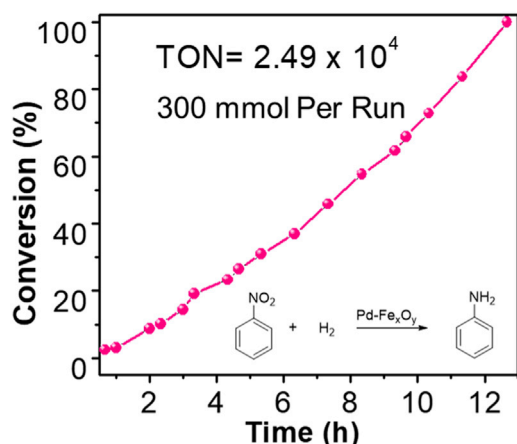


Figure 9. Conversion of Nitrobenzene versus Time in Scale-up Experiment

Reaction conditions: 30 mL nitrobenzene, 20 mg Pd- Fe_xO_y , temperature at 80°C, and H₂ 20 bar.

With the good activity, selectivity and stability of Pd- Fe_xO_y on hand, this catalyst was further tested in a scale-up experiment, during which 30 mL nitrobenzene without solvents was hydrogenated by 20 mg Pd- Fe_xO_y catalyst. The plot of nitrobenzene conversion versus time was shown in Figure 9. Aniline was the main product under solvent-free condition with a high selectivity above 98% (by gas chromatography, GC). The conversion of nitrobenzene was approximately proportional to reaction time, indicating the reaction might follow zero-order kinetics with respect to nitrobenzene under fixed H₂ pressure, which was consistent with previous reports.⁷⁸ Meanwhile, the Pd- Fe_xO_y catalyst offered a high TON value (mol nitrobenzene converted per mol Pt) of 2.49×10^4 .

After the reaction was over, the aniline could be simply separated and collected by centrifugation, due to the different density of aniline (1.02 g/cm³) and water (1.00 g/cm³), and comparisons of samples before and after centrifugation are shown in Figure S12. The isolated yield of aniline was 90% and the product was characterized by proton nuclear magnetic resonance (¹H NMR) (See Figure S13). By combination of magnetic feature for recycling, high activity and selectivity, and good performance in scale-up process, the Pd- Fe_xO_y catalysts might provide an attractive material for nitrobenzene hydrogenation.

RWGS Reaction

In recent years, carbon dioxide utilization is one of the hottest scientific topics.^{79–81} The RWGS for carbon dioxide hydrogenation to carbon monoxide is a promising catalytic process.⁸² Through Fischer-Tropsch synthesis, the obtained CO can be further converted into a variety of liquid fuels (gasoline, diesel, and methanol) and high value oxygenates.^{76,83} In general, catalysts which offer excellent reaction rates in forward reaction also show high reaction rate in reverse reaction. Although Pt-based catalysts were widely used in WGS reaction, there is still large room to optimize the catalytic activity in RWGS reaction. On the other hand, the highly porous Cr₂O₃ with a SSA of 224 m²/g might serve as a potential oxide support, which would promote dispersion of Pt. Therefore, the Pt-Cr₂O₃ material was then studied in RWGS.

The catalytic performance of Pt-Cr₂O₃ in RWGS was exhibited in Figure 9. When WHSV was fixed at 20,000 mL·g⁻¹·h⁻¹, the conversion of CO₂ to CO began at a temperature as low as 200°C. With the increase of temperature, the conversion of CO₂ was enhanced. When the reaction temperature arrived at 500°C, the conversion

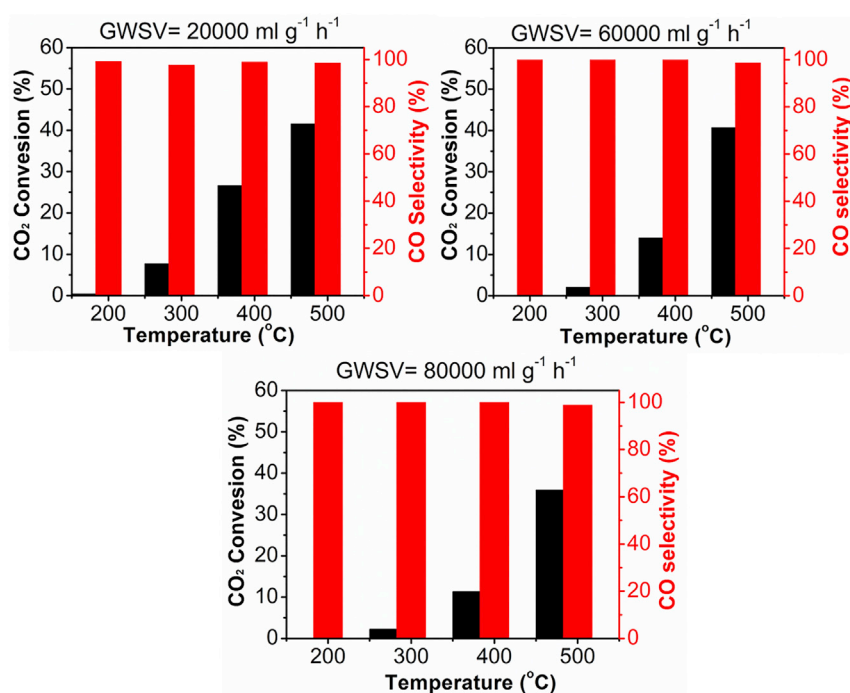


Figure 10. CO₂ Conversion and CO Selectivity of Pt-Cr₂O₃ Catalyst in the RWGS

Reaction conditions: atmospheric pressure, 200°C–500°C; CO₂:H₂=1:3; and WHSV = 20,000; 60,000; and 80,000 mL·g⁻¹·h⁻¹.

of carbon dioxide reached 44%. Besides, the selectivity of CO can keep at more than 98%, when the temperature exceeded 300°C. Moreover, the catalytic performance of Pt-Cr₂O₃ could be maintained at an increased space velocity. Under the conditions of WHSV = 40,000 and 80,000 mL·g⁻¹·h⁻¹, 40% and 35% CO₂ conversion still could be obtained at 500°C (see Figure 10).

Actually, the stability of Cu-based catalysts was often unsatisfying in RWGS,⁸⁴ so we then moved to study the stability of Pt-Cr₂O₃ in CO₂ hydrogenation. Even at 500°C for running for 100 h, both CO₂ conversion and CO selectivity could be maintained (see Figure 11). More importantly, compared with fresh catalyst (average particle size of Pt: 3.2 nm), no evident sintering of Pt NPs was observed after the 100 h CO₂ hydrogenation under a high temperature of 500°C (Figure 11B). The average particle size of reused Pt-Cr₂O₃ catalyst was 4.9 nm. Hence, the highly porous and dispersed Pt-Cr₂O₃ synthesized by NaCl-based solid solution has great potential in a RWGS reaction.

Conclusion

In summary, we have developed a one-pot protocol to fabricate porous metal oxides with fine dispersed noble metal NPs via a NaCl-based solid-solution approach. It was found that the well-dispersion of metal chlorides on NaCl, that is the mechanochemical formation of MCl_x-NaCl, solid solution was a key step to control the porosity of metal oxides and the dispersion of noble metal species. In this regard, a series of porous metal oxides and related catalysts (Fe_xO_y, Cr₂O₃, Co₃O₄, Pd-Fe_xO_y, Pt-Cr₂O₃, and Rh-Co₃O₄) with a high SSA up to 224 m²/g can successfully be prepared. By combination of high SSA and highly dispersed noble metal centers, catalysts obtained by this new route afforded excellent activity and stability in three key redox reactions, such as: CH₄ combustion, hydrogenation of

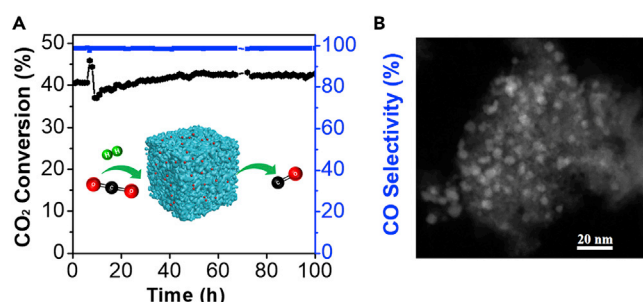


Figure 11. Stability Test of Pt-Cr₂O₃

(A) The performance of Pt-Cr₂O₃ catalyst in the RWGS reaction within 100 h. Reaction conditions:

atmospheric pressure, 500°C; CO₂:H₂ ratio = 1:3; and WHSV = 20,000 mL·g⁻¹·h⁻¹.

(B) The STEM image of Pt-Cr₂O₃ after stability test.

nitrobenzene, and RWGS reaction. A summary comparing the porosities and catalytic activities of the three catalysts with other methods suggests the efficiency of this NaCl-based mechanochemical method (see Table S2). All in all, this simple, effective, and solid state synthesis technique might offer a new way for engineering metal oxide-based catalysts, especially toward large-scale applications.

EXPERIMENTAL PROCEDURES

Resource Availability

Lead Contact

Further information and requests for resources and reagents should be directed to the Lead Contact, Pengfei Zhang (chemistryzpf@sjtu.edu.cn).

Materials Availability

This study did not generate new unique reagents.

Data and Code Availability

This study did not generate datasets or codes.

Full experimental procedures are provided in the [Supplemental Information](#).

SUPPLEMENTAL INFORMATION

Supplemental Information can be found online at <https://doi.org/10.1016/j.chempr.2020.04.003>.

ACKNOWLEDGMENTS

This work was supported by the National Natural Science Foundation of China (21776174), the Thousand Talent Program, the Open Foundation of the State Key Laboratory of Ocean Engineering (Shanghai Jiao Tong University of China) (1809), Shanghai Jiao Tong University Scientific and Technological Innovation Funds (2019QYB06), China Shipbuilding Industry Corporation (CSIC), and Zhejiang Xinan Chemical Industrial Group. H.C., Z.B., Z.W., and S.D. were supported by the U.S. Department of Energy, Office of Science, Office of Basic Energy Sciences, Chemical Sciences, geosciences, and Biosciences Division, Catalysis Science program.

AUTHOR CONTRIBUTIONS

P.Z. and S.D. designed the research idea and experiments. Y.S., N.C., X.D., H.C., Z.B., and Z.W. together completed related experiments, and S.Y. was responsible for the STEM characterization. P.Z. and Y.S. wrote the paper.

DECLARATION OF INTERESTS

The authors declare no competing interests.

Received: November 5, 2019

Revised: January 10, 2020

Accepted: April 2, 2020

Published: April 29, 2020

REFERENCES

- Wang, Y., Arandian, H., Scott, J., Bagheri, A., Dai, H., and Amal, R. (2017). Recent advances in ordered meso/macroporous metal oxides for heterogeneous catalysis: a review. *J. Mater. Chem. A* 5, 8825–8846.
- Liang, J., Zheng, Y., Chen, J., Liu, J., Hulicova-Jurcakova, D., Jaroniec, M., and Qiao, S.Z. (2012). Facile oxygen reduction on a three-dimensionally ordered macroporous graphitic C₃N₄/carbon composite electrocatalyst. *Angew. Chem. Int. Ed.* 51, 3892–3896.
- Taguchi, A., and Schüth, F. (2005). Ordered mesoporous materials in catalysis. *Micropor. Mesopor. Mater.* 77, 1–45.
- Wasalathantri, N.D., Poyraz, A.S., Biswas, S., Meng, Y., Kuo, C.-H., Kriz, D.A., and Suib, S.L. (2015). High-performance catalytic CH₄ oxidation at low temperatures: inverse micelle synthesis of amorphous mesoporous manganese oxides and mild transformation to K_{2-x}Mn₈O₁₆ and ε-MnO₂. *J. Phys. Chem. C* 119, 1473–1482.
- Daniel, M.C., and Astruc, D. (2004). Gold nanoparticles: assembly, supramolecular chemistry, quantum-size-related properties, and applications toward biology, catalysis, and nanotechnology. *Chem. Rev.* 104, 293–346.
- Hvilsted, B., Janssens, T.V.W., Clausen, B.S., Falsig, H., Christensen, C.H., and Nørskov, J.K. (2007). Catalytic activity of Au nanoparticles. *Nano Today* 2, 14–18.
- Haruta, M., and Daté, M. (2001). Advances in the catalysis of Au nanoparticles. *Appl. Catal. A* 222, 427–437.
- Yang, H., and Zhao, D. (2005). Synthesis of replica mesostructures by the nanocasting strategy. *J. Mater. Chem.* 15, 1217–1231.
- Feng, P., Bu, X., and Pine, D.J. (2000). Control of pore sizes in mesoporous silica templated by liquid crystals in block copolymer–cosurfactant–water systems. *Langmuir* 16, 5304–5310.
- Huo, Q., Margolese, D.I., Ciesla, U., Feng, P., Gier, T.E., Sieger, P., Leon, R., Petroff, P.M., Schüth, F., and Stucky, G.D. (1994). Generalized synthesis of periodic surfactant/inorganic composite materials. *Nature* 368, 317–321.
- Alberius, P.C.A., Frindell, K.L., Hayward, R.C., Kramer, E.J., Stucky, G.D., and Chmelka, B.F. (2002). General predictive syntheses of cubic, hexagonal, and lamellar silica and titania mesostructured thin films. *J. Chem. Mater.* 14, 3284–3294.
- Soler-llia, G.J.d.A., Sanchez, C., Lebeau, B., and Patarin, J. (2002). Chemical strategies to design textured materials: from microporous and mesoporous oxides to nanonetworks and hierarchical structures. *Chem. Rev.* 102, 4093–4138.
- Hu, J.S., Zhong, L.S., Song, W.G., and Wan, L.J. (2008). Synthesis of hierarchically structured metal oxides and their application in heavy metal ion removal. *Adv. Mater.* 20, 2977–2982.
- Qian, H., Lin, G., Zhang, Y., Gunawan, P., and Xu, R. (2007). A new approach to synthesize uniform metal oxide hollow nanospheres via controlled precipitation. *Nanotechnology* 18, 355602.
- Tanaka, Y., Utaka, T., Kikuchi, R., Sasaki, K., and Eguchi, K. (2003). CO removal from reformed fuel over Cu/ZnO/Al₂O₃ catalysts prepared by impregnation and coprecipitation methods. *Appl. Catal. A* 238, 11–18.
- Jiang, X., and Wang, T. (2007). Influence of preparation method on morphology and photocatalysis activity of nanostructured TiO₂. *Environ. Sci. Technol.* 41, 4441–4446.
- Li, W.-C., Comotti, M., and Schüth, F. (2006). Highly reproducible syntheses of active Au/TiO₂ catalysts for CO oxidation by deposition-precipitation or impregnation. *J. Catal.* 237, 190–196.
- Ren, L., Wu, Q., Yang, C., Zhu, L., Li, C., Zhang, P., Zhang, H., Meng, X., and Xiao, F.-S. (2012). Solvent-free synthesis of zeolites from solid raw materials. *J. Am. Chem. Soc.* 134, 15173–15176.
- Jin, Y., Sun, Q., Qi, G., Yang, C., Xu, J., Chen, F., Meng, X., Deng, F., and Xiao, F.S. (2013). Solvent-free synthesis of silicoaluminophosphate zeolites. *Angew. Chem. Int. Ed. Engl.* 52, 9172–9175.
- Meng, X., and Xiao, F.S. (2014). Green routes for synthesis of zeolites. *Chem. Rev.* 114, 1521–1543.
- He, X., Deng, Y., Zhang, Y., He, Q., Xiao, D., Peng, M., Zhao, Y., Zhang, H., Luo, R., Gan, T., et al. (2020). Mechanochemical kilogram-scale synthesis of noble metal single-atom catalysts. *Cell Rep. Physiol. Sci.* 1, 100004.
- Tan, D., Loots, L., and Friščić, T. (2016). Towards medicinal mechanochemistry: evolution of milling from pharmaceutical solid form screening to the synthesis of active pharmaceutical ingredients (APIs). *Chem. Commun. (Camb.)* 52, 7760–7781.
- Tan, D., and García, F. (2019). Main group mechanochemistry: from curiosity to established protocols. *Chem. Soc. Rev.* 48, 2274–2292.
- Tan, D., and Friščić, T. (2018). Mechanochemistry for organic chemists: an update. *Eur. J. Org. Chem.* 2018, 18–33.
- Howard, J.L., Cao, Q., and Browne, D.L. (2018). Mechanochemistry as an emerging tool for molecular synthesis: what can it offer? *Chem. Sci.* 9, 3080–3094.
- Do, J.-L., and Friščić, T. (2017). Mechanochemistry: a force of synthesis. *ACS Cent. Sci.* 3, 13–19.
- Biswal, B.P., Chandra, S., Kandambeth, S., Lukose, B., Heine, T., and Banerjee, R. (2013). Mechanochemical synthesis of chemically stable isoreticular covalent organic frameworks. *J. Am. Chem. Soc.* 135, 5328–5331.
- Lu, A.-H., Li, W.-C., Schmidt, W., and Schüth, F. (2006). Fabrication of hierarchically structured carbon monoliths via self-binding and salt templating. *Micropor. Mesopor. Mater.* 95, 187–192.
- Schreyer, H., Eckert, R., Immohr, S., de Bellis, J., Feldhoff, M., and Schüth, F. (2019). Milling down to nanometers: a general process for the direct dry synthesis of supported metal catalysts. *Angew. Chem. Int. Ed.* 58, 11262–11265.
- Danielis, M., Colussi, S., de Leitenburg, C., Soler, L., Llorca, J., and Trovarelli, A. (2018). Outstanding methane oxidation performance of palladium-embedded ceria catalysts prepared by a one-step dry ball-milling method. *Angew. Chem. Int. Ed.* 57, 10212–10216.
- Kamolpop, U., Taylor, S.F.R., Breen, J.P., Burch, R., Delgado, J.J., Chansai, S., Hardacre, C., Hengrasme, S., and James, S.L. (2011). Low-temperature selective catalytic reduction (SCR) of NO_x with n-octane using solvent-free mechanochemically prepared Ag/Al₂O₃ catalysts. *ACS Catal.* 1, 1257–1262.
- Xu, C., De, S., Balu, A.M., Ojeda, M., and Luque, R. (2015). Mechanochemical synthesis of advanced nanomaterials for catalytic applications. *Chem. Commun. (Camb.)* 51, 6698–6713.
- Zhan, W., Yang, S., Zhang, P., Guo, Y., Lu, G., Chisholm, M.F., and Dai, S. (2017). Incorporating rich mesoporosity into a ceria-based catalyst via mechanochemistry. *Chem. Mater.* 29, 7323–7329.
- Zhou, M., Zhao, J., Zhang, P., Chen, N., and Yang, S. (2019). Solvent-free and rapid synthesis of mesoporous Pt–iron oxide catalysts via mechanochemical assembly. *Catal. Sci. Technol.* 9, 3907–3913.

35. Zhang, P., Wang, L., Yang, S., Schott, J.A., Liu, X., Mahurin, S.M., Huang, C., Zhang, Y., Fulvio, P.F., Chisholm, M.F., and Dai, S. (2017). Solid-state synthesis of ordered mesoporous carbon catalysts via a mechanochemical assembly through coordination cross-linking. *Nat. Commun.* 8, 15020.
36. Li, G., Sun, J., Hou, W., Jiang, S., Huang, Y., and Geng, J. (2016). Three-dimensional porous carbon composites containing high sulfur nanoparticle content for high-performance lithium–sulfur batteries. *Nat. Commun.* 7, 10601.
37. Dai, F., Zai, J., Yi, R., Gordin, M.L., Sohn, H., Chen, S., and Wang, D. (2014). Bottom-up synthesis of high surface area mesoporous crystalline silicon and evaluation of its hydrogen evolution performance. *Nat. Commun.* 5, 3605.
38. Fechler, N., Fellinger, T.P., and Antonietti, M. (2013). “Salt templating”: a simple and sustainable pathway toward highly porous functional carbons from ionic liquids. *Adv. Mater.* 25, 75–79.
39. Wei, N., Yu, L., Sun, Z., Song, Y., Wang, M., Tian, Z., Xia, Y., Cai, J., Li, Y.Y., Zhao, L., et al. (2019). Scalable salt-templated synthesis of nitrogen-doped graphene nanosheets toward printable energy storage. *ACS Nano* 13, 7517–7526.
40. Yang, J., Feng, X., Lu, G., Li, Y., Mao, C., Wen, Z., and Yuan, W. (2018). NaCl as a solid solvent to assist the mechanochemical synthesis and post-synthesis of hierarchical porous MOFs with high I_2 vapour uptake. *Dalton Trans* 47, 5065–5071.
41. Kleger, N., Cihova, M., Masania, K., Studart, A.R., and Löfller, J.F. (2019). 3D printing of salt as a template for magnesium with structured porosity. *Adv. Mater.* 31, e1903783.
42. Xiao, X., Song, H., Lin, S., Zhou, Y., Zhan, X., Hu, Z., Zhang, Q., Sun, J., Yang, B., Li, T., et al. (2016). Scalable salt-templated synthesis of two-dimensional transition metal oxides. *Nat. Commun.* 7, 11296.
43. Hu, Z., Xiao, X., Jin, H., Li, T., Chen, M., Liang, Z., Guo, Z., Li, J., Wan, J., Huang, L., et al. (2017). Rapid mass production of two-dimensional metal oxides and hydroxides via the molten salts method. *Nat. Commun.* 8, 15630.
44. Liu, X., Giordano, C., and Antonietti, M. (2012). A molten-salt route for synthesis of Si and Ge nanoparticles: chemical reduction of oxides by electrons solvated in salt melt. *J. Mater. Chem.* 22, 5454–5459.
45. Bale, C.W., Chartrand, P., Degterov, S.A., Eriksson, G., Hack, K., Ben Mahfoud, R.B., Melançon, J., Pelton, A.D., and Petersen, S. (2002). FactSage thermochemical software and databases. *Calphad* 26, 189–228.
46. Gu, D., and Schüth, F. (2014). Synthesis of non-siliceous mesoporous oxides. *Chem. Soc. Rev.* 43, 313–344.
47. Liu, H., Xue, Q., Zhao, J., and Zhang, Q. (2018). Enhanced supercapacitive performance of binary cooperative complementary $\text{Co(OH)}_2/\text{Mn}_3\text{O}_4$ nanomaterials directly synthesized through ion diffusion method controlled by ion exchange membrane. *Electrochim. Acta* 260, 330–337.
48. Chen, X., Chen, X., Cai, S., Chen, J., Xu, W., Jia, H., and Chen, J. (2018). Catalytic combustion of toluene over mesoporous Cr_2O_3 -supported platinum catalysts prepared by in situ pyrolysis of MOFs. *Chem. Eng. J.* 334, 768–779.
49. Tüysüz, H., Weidenthaler, C., Grewe, T., Salabaş, E.L., Benítez Romero, M.J., and Schüth, F. (2012). A crystal structure analysis and magnetic investigation on highly ordered mesoporous Cr_2O_3 . *Inorg. Chem.* 51, 11745–11752.
50. Liu, H., Du, X., Xing, X., Wang, G., and Qiao, S.Z. (2012). Highly ordered mesoporous Cr_2O_3 materials with enhanced performance for gas sensors and lithium ion batteries. *Chem. Commun. (Camb.)* 48, 865–867.
51. Li, L., Zhu, Z., Yao, X., Lu, G., and Yan, Z. (2008). Synthesis and characterization of chromium oxide nanocrystals via solid thermal decomposition at low temperature. *Micropor. Mesopor. Mater.* 112, 621–626.
52. Zhang, P., Gong, Y., Wei, Z., Wang, J., Zhang, Z., Li, H., Dai, S., and Wang, Y. (2014). Updating biomass into functional carbon material in ionothermal manner. *ACS Appl. Mater. Interfaces* 6, 12515–12522.
53. Ma, Z., Yu, J., and Dai, S. (2010). Preparation of inorganic materials using ionic liquids. *Adv. Mater.* 22, 261–285.
54. Liu, L., Li, Y., Wei, H., Dong, M., Wang, J., Slawin, A.M., Li, J., Dong, J., and Morris, R.E. (2009). Ionothermal synthesis of zirconium phosphates and their catalytic behavior in the selective oxidation of cyclohexane. *Angew. Chem. Int. Ed.* 48, 2206–2209.
55. Bruix, A., Lykhach, Y., Matolínová, I., Neitzel, A., Skála, T., Tsud, N., Vorokhta, M., Stetsovich, V., Ševčíková, K., Mysliveček, J., et al. (2014). Maximum noble-metal efficiency in catalytic materials: atomically dispersed surface platinum. *Angew. Chem. Int. Ed.* 53, 10525–10530.
56. Duan, H., Xu, D., Li, W., and Xu, H. (2008). Study of the redox properties of noble metal/ Co_3O_4 by electrical conductivity measurements. *Catal. Lett.* 124, 318–323.
57. Dacquin, J.-P., Dujardin, C., and Granger, P. (2008). Surface reconstruction of supported Pd on LaCoO_3 : consequences on the catalytic properties in the decomposition of N_2O . *J. Catal.* 253, 37–49.
58. Xia, P., Zuo, S., Liu, F., and Qi, C. (2013). Ceria modified crystalline mesoporous Cr_2O_3 based nanocomposites supported metal oxide for benzene complete oxidation. *Catal. Commun.* 41, 91–95.
59. Boudart, M., and Hwang, H. (1975). Solubility of hydrogen in small particles of palladium. *J. Catal.* 39, 44–52.
60. Zhu, M., Tian, P., Chen, J., Ford, M.E., Xu, J., Wachs, I.E., and Han, Y.F. (2020). Activation and deactivation of the commercial-type $\text{CuO}-\text{Cr}_2\text{O}_3-\text{Fe}_2\text{O}_3$ high temperature shift catalyst. *AIChE J.* 66, e16846.
61. Howarth, R.W., Santoro, R., and Ingraffea, A. (2011). Methane and the greenhouse-gas footprint of natural gas from shale formations. *Clim. Change* 106, 679–690.
62. Xiao, L.-h., Sun, K.-p., Xu, X.-l., and Li, X.-n. (2005). Low-temperature catalytic combustion of methane over Pd/CeO_2 prepared by deposition–precipitation method. *Catal. Commun.* 6, 796–801.
63. Hu, W., Lan, J., Guo, Y., Cao, X.-M., and Hu, P. (2016). Origin of efficient catalytic combustion of methane over Co_3O_4 (110) active low-coordination lattice oxygen and cooperation of multiple active sites. *ACS Catal.* 6, 5508–5519.
64. Wu, Z., Deng, J., Liu, Y., Xie, S., Jiang, Y., Zhao, X., Yang, J., Arandiyam, H., Guo, G., and Dai, H. (2015). Three-dimensionally ordered mesoporous Co_3O_4 -supported Au–Pd alloy nanoparticles: high-performance catalysts for methane combustion. *J. Catal.* 332, 13–24.
65. Wang, H., Chen, C., Zhang, Y., Peng, L., Ma, S., Yang, T., Guo, H., Zhang, Z., Su, D.S., and Zhang, J. (2015). In situ oxidation of carbon-encapsulated cobalt nanocapsules creates highly active cobalt oxide catalysts for hydrocarbon combustion. *Nat. Commun.* 6, 7181.
66. Tanaka, H., Taniguchi, M., Uenishi, M., Kajita, N., Tan, I., Nishihata, Y., Mizuki, J.i., Narita, K., Kimura, M., and Kaneko, K. (2006). Self-regenerating Rh-and Pt-based perovskite catalysts for automotive-emissions control. *Angew. Chem. Int. Ed.* 45, 5998–6002.
67. Maestri, M., Vlachos, D.G., Beretta, A., Groppi, G., and Tronconi, E. (2009). A C1 microkinetic model for methane conversion to syngas on $\text{Rh}/\text{Al}_2\text{O}_3$. *AIChE J.* 55, 993–1008.
68. Shan, J., Li, M., Allard, L.F., Lee, S., and Flytzani-Stephanopoulos, M. (2017). Mild oxidation of methane to methanol or acetic acid on supported isolated rhodium catalysts. *Nature* 551, 605–608.
69. Ma, J., Lou, Y., Cai, Y., Zhao, Z., Wang, L., Zhan, W., Guo, Y., and Guo, Y. (2018). The relationship between the chemical state of Pd species and the catalytic activity for methane combustion on Pd/CeO_2 . *Catal. Sci. Technol.* 8, 2567–2577.
70. Willis, J.J., Goodman, E.D., Wu, L., Riscoe, A.R., Martins, P., Tassone, C.J., and Cargnello, M. (2017). Systematic identification of promoters for methane oxidation catalysts using size-and composition-controlled Pd-based bimetallic nanocrystals. *J. Am. Chem. Soc.* 139, 11989–11997.
71. Cargnello, M., Delgado Jaén, J.J., Hernández Garrido, J.C., Bakhmutsky, K., Montini, T., Calvino Gámez, J.J., Gorte, R.J., and Fornasier, P. (2012). Exceptional activity for methane combustion over modular $\text{Pd}@\text{CeO}_2$ subunits on functionalized Al_2O_3 . *Science* 337, 713–717.
72. Han, C.W., Majumdar, P., Marinero, E.E., Aguilar-Tapia, A., Zanella, R., Greeley, J., and Ortalan, V. (2015). Highly stable bimetallic Au/TiO_2 catalyst: physical origins of the intrinsic high stability against sintering. *Nano Lett.* 15, 8141–8147.
73. Wang, J., Yuan, Z., Nie, R., Hou, Z., and Zheng, X. (2010). Hydrogenation of nitrobenzene to aniline over silica gel supported nickel catalysts. *Ind. Eng. Chem. Res.* 49, 4664–4669.

74. Jiang, T., Du, S., Jafari, T., Zhong, W., Sun, Y., Song, W., Luo, Z., Hines, W.A., and Suib, S.L. (2015). Synthesis of mesoporous γ -Fe₂O₃ supported palladium nanoparticles and investigation of their roles as magnetically recyclable catalysts for nitrobenzene hydrogenation. *Appl. Catal. A* 502, 105–113.
75. Chen, P., Khetan, A., Yang, F., Migunov, V., Weide, P., Stürmer, S.P., Guo, P., Kähler, K., Xia, W., Mayer, J., et al. (2017). Experimental and theoretical understanding of nitrogen-doping-induced strong metal-support interactions in Pd/TiO₂ catalysts for nitrobenzene hydrogenation. *ACS Catal.* 7, 1197–1206.
76. Zhai, P., Xu, C., Gao, R., Liu, X., Li, M., Li, W., Fu, X., Jia, C., Xie, J., Zhao, M., et al. (2016). Highly tunable selectivity for syngas-derived alkenes over zinc and sodium-modulated Fe₅C₂ catalyst. *Angew. Chem. Int. Ed.* 55, 9902–9907.
77. Sun, J., Fu, Y., He, G., Sun, X., and Wang, X. (2014). Catalytic hydrogenation of nitrophenols and nitrotoluenes over a palladium/graphene nanocomposite. *Catal. Sci. Technol.* 4, 1742–1748.
78. Turáková, M., Salmi, T., Eränen, K., Wärnå, J., Murzin, D.Y., and Králík, M. (2015). Liquid phase hydrogenation of nitrobenzene. *Appl. Catal. A* 499, 66–76.
79. Gao, S., Lin, Y., Jiao, X., Sun, Y., Luo, Q., Zhang, W., Li, D., Yang, J., and Xie, Y. (2016). Partially oxidized atomic cobalt layers for carbon dioxide electroreduction to liquid fuel. *Nature* 529, 68–71.
80. Studt, F., Sharafutdinov, I., Abild-Pedersen, F., Elkjær, C.F., Hummelshøj, J.S., Dahl, S., Chorkendorff, I., and Nørskov, J.K. (2014). Discovery of a Ni-Ga catalyst for carbon dioxide reduction to methanol. *Nat. Chem.* 6, 320–324.
81. Kattel, S., Ramírez, P.J., Chen, J.G., Rodriguez, J.A., and Liu, P. (2017). Active sites for CO₂ hydrogenation to methanol on Cu/ZnO catalysts. *Science* 355, 1296–1299.
82. Porosoff, M.D., Yang, X., Boscoboinik, J.A., and Chen, J.G. (2014). Molybdenum carbide as alternative catalysts to precious metals for highly selective reduction of CO₂ to CO. *Angew. Chem. Int. Ed.* 53, 6705–6709.
83. Omae, I. (2012). Recent developments in carbon dioxide utilization for the production of organic chemicals. *Coord. Chem. Rev.* 256, 1384–1405.
84. Yue, H., Zhao, Y., Zhao, S., Wang, B., Ma, X., and Gong, J. (2013). A copper-phyllosilicate core-sheath nanoreactor for carbon–oxygen hydrogenolysis reactions. *Nat. Commun.* 4, 2339.